Draft version November 2, 2023
Typeset using LaTeX **twocolumn** style in AASTeX62

Partial Eruption of Solar Filaments. I. Configuration and Formation of Double-decker Filaments

Yijun Hou,[1,2,3,4] Chuan Li,[5,6] Ting Li,[1,3,4] Jiangtao Su,[1,3,4] Ye Qiu,[5,6] Shuhong Yang,[1,3,4] Liheng Yang,[7,2] Leping Li,[1,3,4] Yilin Guo,[8] Zhengyong Hou,[9] Qiao Song,[10,11] Xianyong Bai,[1,3,4] Guiping Zhou,[1,3,4] Mingde Ding,[5,6] Weiqun Gan,[12] and Yuanyong Deng[1,3,4]

[1] *National Astronomical Observatories, Chinese Academy of Sciences, Beijing 100101, China*
[2] *Yunnan Key Laboratory of the Solar physics and Space Science, Kunming, 650216, China*
[3] *State Key Laboratory of Solar Activity and Space Weather, Beijing, 100190, China*
[4] *School of Astronomy and Space Science, University of Chinese Academy of Sciences, Beijing 100049, China*
[5] *School of Astronomy and Space Science, Nanjing University, Nanjing 210023, China*
[6] *Key Laboratory of Modern Astronomy and Astrophysics (Nanjing University), Ministry of Education, Nanjing 210023, China*
[7] *Yunnan Observatories, Chinese Academy of Sciences, Kunming, 650216, China*
[8] *Beijing Planetarium, Beijing Academy of Science and Technology, Beijing 100044, China*
[9] *School of Earth and Space Sciences, Peking University, Beijing 100871, China*
[10] *Key Laboratory of Space Weather, National Satellite Meteorological Center (National Center for Space Weather), China Meteorological Administration, Beijing 100081, China*
[11] *Innovation Center for FengYun Meteorological Satellite (FYSIC), Beijing 100081, China*
[12] *Purple Mountain Observatory, Chinese Academy of Sciences, Nanjing 210034, China*

ABSTRACT

Partial eruptions of solar filaments are the typical representative of solar eruptive behavior diversity. Here we investigate a typical filament partial eruption event and present integrated evidence for configuration of the pre-eruption filament and its formation. The *CHASE* Hα observations reveal structured Doppler velocity distribution within the pre-eruption filament, where distinct redshift only appeared in the east narrow part of the south filament region and then disappeared after the partial eruption while the north part dominated by blueshift remained. Combining the *SDO*, *ASO-S* observations, and NLFFF modeling results, we verify that there were two independent material flow systems within the pre-flare filament, whose magnetic topology is a special double-decker configuration consisting of two magnetic flux ropes (MFRs) with opposite magnetic twist. During the formation of this filament system, continuous magnetic flux cancellation and footpoint motion were observed around its north end. Therefore, we propose a new double-decker formation scenario that the two MFRs composing such double-decker configuration originated from two magnetic systems with different initial connections and opposite magnetic twist. Subsequent magnetic reconnection with surrounding newly-emerging fields resulted in the motion of footpoint of the upper MFR to the region around footpoint of the lower MFR, thus leading to eventual formation of the double-decker configuration consisting of two MFRs with similar footpoints but opposite signs of magnetic twist. These results provide a potential way to determine unambiguously the progenitor configuration of a partial-eruptive filament and reveal a special type of double-decker MFR configuration and a new double-decker formation scenario.

Keywords: Solar activity (1475); Solar atmosphere (1477); Solar filaments (1495); Solar flares (1496); Solar magnetic fields (1503)

1. INTRODUCTION

On the solar disk, elongated dark absorption features are often seen in Hα and extreme ultraviolet (EUV) observations and are called "solar filaments". When moving to the solar limb, solar filaments appear as bright emission structures suspended in the corona and are described as "prominences" (Mackay et al. 2010; Chen et al. 2020). Solar filaments are related to abundant physical processes and multi-scale activities occurring in solar at-

Corresponding author: Yijun Hou
yijunhou@nao.cas.cn

mosphere, e.g., thermal instabilities during the filament formation (Antiochos & Klimchuk 1991; Xia et al. 2011; Zhou et al. 2020), oscillations of the filament threads (Oliver & Ballester 2002; Li & Zhang 2012; Antolin et al. 2015), and various types of small-scale activities induced by magnetohydrodynamic (MHD) instabilities or magnetic reconnection (Shen et al. 2015; Berger et al. 2017; Li et al. 2018; Wang et al. 2022; Jenkins & Keppens 2022). Especially, filament eruptions are closely related to solar flares and coronal mass ejections (CMEs), which can pose disastrous disturbances to the space environment near the Earth. As a result, solar filaments are the ideal object for studying magnetic and plasma structures of corona and their evolutions, mass and energy transportations between different solar atmospheric layers, as well as the driving mechanisms of solar eruptions.

Solar filaments usually lie along the polarity inversion line (PIL) separating photospheric magnetic fields with opposite radial components. As regards the magnetic topology of solar filaments, there are two typical models: the sheared arcade model for the normal-polarity filaments and the magnetic flux rope (MFR, a helical structure of magnetic field lines wrapping more than once around a central axis) model for the inverse-polarity filaments (Aulanier et al. 2002; Mackay et al. 2010; Liu et al. 2016). In both models, the filament plasmas are pilled at magnetic dips, where magnetic tension supports plasmas against their gravity. It is worth noting that an MFR and a sheared arcade could co-exist in one solar filament and match two sections of the filament, respectively (Guo et al. 2010).

Triggered by several possible mechanisms, e.g., magnetic-reconnection-related processes (Chen & Shibata 2000; Zhang et al. 2001; Sterling & Moore 2004; Dacie et al. 2018; Song et al. 2020; Hou et al. 2020b) and ideal MHD instabilities (Török & Kliem 2005; Démoulin & Aulanier 2010; Yang et al. 2017b; Hou et al. 2018; Zou et al. 2020), filaments could lose the balance of forces acting on them and eventually erupt. In the classical solar eruption scenarios (e.g., CSHKP model), filament eruptions play a critical role in the onset of solar flares and CMEs. It is well established that an erupting filament will push its overlying magnetic fields upwards and form a reconnection region below, where particles are accelerated and propagate downward along the newly formed magnetic fields, hitting the lower solar atmosphere and producing flare ribbons. When the erupting filament successfully escapes the solar atmosphere, a CME would be produced (Lin & Forbes 2000; Priest & Forbes 2002; Schmieder et al. 2013).

Previous high-resolution observations have revealed that solar filaments exhibit a wide range of eruptive dynamics. Gilbert et al. (2007) developed observational definitions for three types of filament eruptions: (1) "full eruption", the magnetic structure and material of pre-eruptive filament completely escape the Sun; (2) "failed eruption", the eruptive process of filament is suddenly halted in the low corona, with none of the lifted filament material nor magnetic structure escaping the Sun (Ji et al. 2003; Török & Kliem 2005; Myers et al. 2015; Li & Ding 2017; Yan et al. 2020); (3) "partial eruption", only part of the filament magnetic structure and/or material is eventually expelled (Gilbert et al. 2000; Zhang et al. 2015; Bi et al. 2015; Chen et al. 2018; Dai et al. 2022). Among the three types, filament partial eruptions are relatively more complicated because the involved pre-eruption filament does not evolve as a whole and shows nonuniform characteristics in terms of magnetic topology and/or plasma motion.

Regarding the mechanism of filament partial eruptions, two main physical scenarios are proposed by observational and numerical studies. The first one was proposed by Gibson & Fan (2006) through three-dimensional (3D) MHD modeling that the magnetic structure of the pre-eruption filament is an MFR with a bald patch (BP), where the bottom magnetic field lines of MFR touch the photosphere tangentially. During the eruption of this MFR, the magnetic field lines tying in the BP prevent the lower part of the MFR from erupting, naturally leading to internal magnetic reconnection within the MFR and subsequent vertical splitting of the MFR into two parts, with one part successfully being expelled and the other one remaining behind (Gilbert et al. 2001). This mechanism has been further supported by observations of splitting process accompanied by obvious local brightening between the erupting and remaining parts of the filament (Tripathi et al. 2009, 2013; Cheng et al. 2018; Hu et al. 2022; Sun et al. 2023). In addition, solar filaments are also observed to split under the interaction with surrounding magnetic structures. For example, Xue et al. (2023) reported a filament splitting event caused by the reconnection of emerging magnetic fields with one leg of the pre-eruption filament. Similar splitting processes driven by such reconnection with surrounding structures could also further result in partial eruptions of solar filaments (Chen et al. 2018; Monga et al. 2021; Dai et al. 2022).

The second scenario for the filament partial eruption is the double-decker model proposed by Liu et al. (2012), which was later simulated by Kliem et al. (2014). In this model, the magnetic structure of the pre-eruption filament consists of two vertically-distributed parts:

two separate MFRs or one MFR above sheared arcades. Observations have revealed that such partially erupting filament is composed of two branches separated in height, which have already existed several hours prior to the eruption. Intermittent transfers of magnetic flux and current from the lower branch to the upper one serve as the key mechanism for the upper branch to lose equilibrium and erupt eventually (Liu et al. 2012; Zhu & Alexander 2014). This scenario has also been supported by observations and nonlinear-force-free-field (NLFFF) extrapolation results in following studies (Cheng et al. 2014; Hou et al. 2018, 2020a; Awasthi et al. 2019; Zheng et al. 2019; Mitra et al. 2020; Pan et al. 2021; Chen et al. 2021; Zhang et al. 2022b).

Although the partial eruptions of solar filaments have been extensively investigated over the past decades, our knowledge of this kind of filament eruption is continuously updated, and several open questions still remain: How can we determine unambiguously which mechanism is responsible for the observed filament partial eruption? Can the two mechanisms introduced above simultaneously play roles during the partial eruption of filament? Is there another type of double-decker configuration different from the typical ones existing in the filament partial eruption event? How does this type of double-decker configuration form and evolve into eruption? Insights into these questions are necessary to further understand the eruptive behavior diversity and magnetic topology complexity of solar filaments.

In the present work, we investigate a typical filament partial eruption event and present integrated evidence for the double-decker configuration of pre-eruption filament and its formation process from the aspects of material flow pattern, magnetic topology, and their morphological evolutions. The data from the *Chinese Hα Solar Explorer* (*CHASE*; Li et al. 2022), *Solar Dynamics Observatory* (*SDO*; Pesnell et al. 2012), *Advanced Space-based Solar Observatory* (*ASO-S*; Gan et al. 2023), and other instruments are analyzed, aided by the NLFFF extrapolations with a time sequence, to reveal configuration and formation of this double-decker filament system. The remainder of this paper is structured as follows. Section 2 describes the observations and data analysis methods taken in our study. In Section 3, the results of observations and analysis are presented and discussed. Finally, we briefly summarize the major findings in Section 4.

2. OBSERVATIONS AND DATA ANALYSIS

The filament partial eruption event of interest occurred in NOAA AR 13176 on 2022 December 30 and was well observed by the *CHASE*, *SDO*, and *ASO-S*. Additionally, the EUV images taken by the Solar Upper Transition Region Imager (SUTRI; Bai et al. 2023) on board the first spacecraft of the Space Advanced Technology demonstration satellite series (*SATech-01*), Chinese Academy of Sciences (CAS) and the Solar X-ray and Extreme Ultraviolet Imager (*X-EUVI*) on board the *FengYun-3E* (*FY-3E*; Zhang et al. 2022a), satellite, and the soft X-ray (SXR) 1–8 Å flux from the *GOES* were also employed. The details of these observations are summarized in Table 1.

The *CHASE*, launched on 2021 October 14, is the first solar space mission of China National Space Administration (CNSA). The Hα Imaging Spectrograph (HIS; Liu et al. 2022) is the scientific payload of the *CHASE* and can provide spectroscopic observations of the Sun by scanning the full solar disk in both Hα (6559.7–6565.9 Å) and Fe I (6567.8–6570.6 Å) wavebands. The *CHASE*/HIS data applied here have been calibrated through dark-field, flat-field, and slit image curvature corrections, wavelength and intensity calibration, and coordinate transformation (Qiu et al. 2022). Since the Hα line profiles are roughly symmetrical, we adopted the moment analysis to obtain Doppler velocity of the filament, i.e., $\lambda_0 = \frac{\sum \lambda_i (I_i - I_c)}{\sum (I_i - I_c)}$, where I_c is the continuum intensity, I_i and λ_0 are the intensity and calculated gravity center of the observed Hα line profile. The zero Doppler shift is defined as the gravity center of the averaged profile in a quiescent region [-80″, -68″]×[385″, 395″]. The uncertainty is then estimated as the root mean square of velocity of this region, which are 0.37 km s^{-1} and 0.36 km s^{-1} at 19:03:07 UT and 20:27:24 UT, respectively.

The *ASO-S* is the first comprehensive Chinese dedicated solar observatory in space and its primary scientific objective is to improve our understanding of solar flares, CMEs, solar magnetic fields, and the relationships among them. The Full-disk vector MagnetoGraph (FMG; Deng et al. 2019) on board the *ASO-S* is designed to measure the solar photospheric magnetic fields through Fe I 532.42 nm line with high spatial and temporal resolutions, and high magnetic sensitivity. Here we utilized the line-of-sight (LOS) magnetograms and filtergram of Fe I 532.42 nm line taken by the *ASO-S*/FMG. Furthermore, the EUV images at Ne VII 46.5 nm with a formation temperature of ∼0.5 MK and Fe XII 19.5 nm line of ∼1.5 MK observed by *SATech-01*/SUTRI and *FY-3E*/X-EUVI, respectively, are also analyzed to show the M3.7 flare caused by the filament partial eruption event.

The Atmospheric Imaging Assembly (AIA; Lemen et al. 2012) and Helioseismic and Magnetic Imager (HMI;

Table 1. Details of the data analyzed in this study

Telescope	Time (UT)	Passband & Data product	Cadence	Spatial & Spectral resolutions
CHASE/HIS	18:48–19:04	Imaging data of Hα 6562.8 Å	~71 s	~1.0″ pixel^{-1}
		Spectra data of Hα 6562.8 Å	~71 s	~0.048 Å pixel^{-1}
	20:23–20:39	Imaging data of Hα 6562.8 Å	~71 s	~1.0″ pixel^{-1}
		Spectra data of Hα 6562.8 Å	~71 s	~0.048 Å pixel^{-1}
ASO-S/FMG	10:07–20:30	LOS magnetogram	~116 s	~0.5″ pixel^{-1}
	10:07–20:30	Filtergram of Fe I 5324.2 Å	~116 s	~0.5″ pixel^{-1}
SDO/AIA	00:00–20:30	304, 171, 94 Å	12 s	~0.6″ pixel^{-1}
SDO/HMI	00:00–20:30	Full-disk vector magnetograms	720 s	~0.5″ pixel^{-1}
	00:00–20:30	LOS magnetogram	45 s	~0.5″ pixel^{-1}
SATech-01/SUTRI	19:38	465 Å	/	~1.2″ pixel^{-1}
FY-3E/X-EUVI	19:43	195 Å	/	~2.4″ pixel^{-1}
GOES/EXIS	18:30–21:00	soft X-ray (SXR) flux of 1–8 Å	60 s	/

Schou et al. 2012) on board the *SDO* can successively observe the multilayered solar atmosphere in ten passbands and the photospheric magnetic field, respectively. Here, we analyzed the AIA 304 Å, 171 Å, and 94 Å images as well as the HMI LOS magnetograms and photospheric vector magnetic field. The *CHASE*, *SDO*, *ASO-S*, SUTRI, and X-EUVI observations are carefully co-aligned by matching locations of some specific features that can be simultaneously detected in different channels of these telescopes.

In order to reconstruct the 3D magnetic configuration above the region of interest, we utilized the "weighted optimization" method to perform NLFFF extrapolation (Wiegelmann 2004; Wiegelmann et al. 2012) based on the photospheric vector magnetic fields observed by *SDO*/HMI. Before extrapolation calculation, the HMI vector magnetograms were preprocessed by a procedure developed by Wiegelmann et al. (2006) towards suitable photospheric boundary conditions consistent with the force-free assumption. Then the calculations were performed within a box of 720×448×256 uniform grid points (261×163×93 Mm^3), which covers nearly the entire AR. Furthermore, through the method developed by Liu et al. (2016), we calculated the twist number T_w and squashing factor Q of the extrapolated 3D magnetic fields. The squashing factor Q provides important information about the magnetic connectivity, and the twist number T_w represents how many turns two field lines wind about each other and plays a critical role in identifying an MFR without ambiguity.

3. RESULTS AND DISCUSSION

3.1. *Overview of the filament partial eruption event*

The event of interest took place around the main sunspot of NOAA AR 13176 (see Figure 1 and the associated online animation). On 2022 December 30, this AR approached the solar disk center, and there were several filaments around the main sunspot of the AR. As shown in Figures 1(a), (c), and (d), the filament studied here was located to the northwest of the sunspot, with its south end rooted on the sunspot region with positive magnetic polarity and the north one on a negative-polarity region to the north of the sunspot. Subsequently, this filament (hereafter "pre-flare filament") erupted and produced an M3.7 flare (peaked at 19:38 UT) with a smaller precursor C4.0 flare (peaked at 19:10 UT). Because the *CHASE* observations (18:48–19:04 UT and 20:23–20:39 UT) did not cover the main phase of the flare, we can only see the target region before and after the eruption with *CHASE*/HIS Hα images. It is revealed that there was still a filament (hereafter "post-flare filament") to be left in the flare core region at 20:27 UT after the eruption of pre-flare filament (see Figure 1(b)). Figures 1(e)–(h) show that the M3.7 flare produced by the filament partial eruption event exhibited typical compact flare loops and multiple flare ribbons observed in different EUV channels with temperatures ranging from 0.5 MK to 6.3 MK. As a result, we can conclude that the pre-flare filament underwent a partial eruption process and produced an M3.7 flare.

As introduced in Section 1, the partial eruption of solar filaments could be mainly produced through two scenarios: (1) the vertical splitting of one MFR caused by internal magnetic reconnection, and (2) the eruption of upper MFR in a double-decker system containing two separate vertically-distributed parts. It is obvious that the most significant difference between the two scenarios is reflected in the magnetic configuration of the pre-eruption filament system. To unambiguously determine which mechanism is dominant in the event reported here, three aspects of the pre-eruption filament

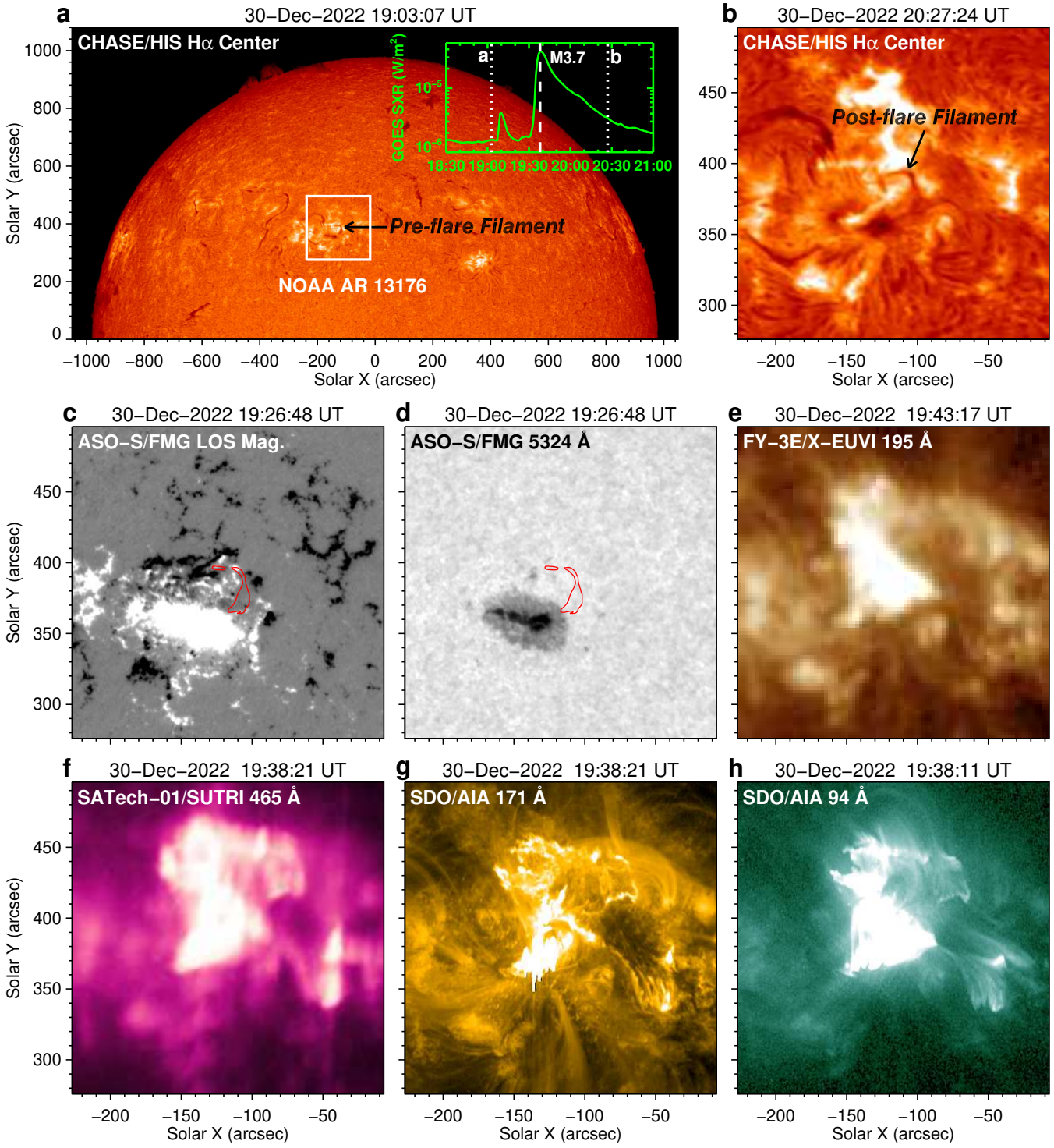

Figure 1. Overview of the filament partial eruption event and the resultant M3.7 flare on 2022 December 30. (a)–(b): *CHASE*/HIS Hα center (6562.8 Å) images showing the filament of interest before and after the M3.7 flare. The overlaied *GOES* SXR 1–8 Å flux variation reveals the M3.7 flare caused by the filament partial eruption. (c)–(d): *ASO-S*/FMG LOS magnetogram and filtergram of Fe I 5324 Å exhibiting the photospheric magnetic environment of the erupting filament. The red contours outline the fragments of pre-eruption filament observed in Hα channel. (e)–(h): *FY-3E*/EUVI 195 Å, *SATech-01*/SUTRI 465 Å, *SDO*/AIA 171 Å, and 94 Å images showing the M3.7 flare in different channels around its peak time. An animation (Figure1.mp4) covering 19:00 UT to 20:25 UT on December 30 is available online, which presents the filament partial eruption in AIA 304, 171, 193, and 94 Å channels. The animation's duration is 12 seconds.

are needed to consider at least: material flow pattern, magnetic structure, and their temporal evolutions.

3.2. *Configuration of the double-decker filament system*

3.2.1. *Material flow patterns in the double-decker filament system*

To investigate mass motions of the filament system, we analyzed the *CHASE*/HIS spectroscopic observations at the Hα waveband. As shown in Figures 2(a1)–(a3), before the eruption, the pre-flare filament manifests as dark absorption features with different spatial distributions in the images of Hα line center and two wings. The filament system has a shape of the number "7" in the Hα center image and its south part is much wider than the north part. In the Hα blue wing (-0.5 Å) image, only the north part of the filament is visible. While in the Hα red wing (+0.5 Å) image, the southeast narrow part of the filament is obvious. Furthermore, the Doppler velocity map derived from Hα spectra data reveals that in the south part of the filament, strong redshift signal (about 8 km s^{-1}) only appears in the east narrow part. The north region of the filament is partially dominated by blueshift of 4–6 km s^{-1} (see the blue and red quadrilaterals in panel (a4)). Figures 2(b1)–(b4) show that after the partial eruption, the north part of the filament system and the associated blueshift signal are still visible but with a much narrower spatial scale. Meanwhile, in the south region, the filament absorption feature and redshift Doppler signal are all absent.

Material flows in a filament system can provide critical clues about its host magnetic structures. It is thus reasonable to expect that filaments with different magnetic topologies will express different flow patterns. For example, in the filament with a single uniform magnetic configuration, Doppler redshift and blueshift signals will be distributed randomly due to counter-streaming flows in different filament threads (Zirker et al. 1998; Zhou et al. 2020) or regularly detected at the opposite sides of the filament spine over a large spatial range due to the rotation motion of the filament material along the twisted field of an MFR (Awasthi et al. 2019). But in the event reported here, the structured distributions of redshift and blueshift within the pre-flare filament do not show typical characteristics of a single uniform magnetic configuration as mentioned above. Instead, the fact that redshift only appears in the east narrow part of the south region indicates that there could be two separate material flow patterns within the filament system, at least in the south region. Furthermore, the disappearance of the southeast narrow part of the filament system dominated by redshift and the invariableness of the north part dominated by blueshift after the partial eruption suggest that the region of redshift and the region of blueshift could be two separate material flow systems within the filament.

Based on the successive EUV images obtained by *SDO*/AIA, we further investigated the material structure of the filament system by analyzing its temporal evolution during the M3.7 flare. In AIA 304 Å observations, the pre-flare filament shows the similar morphology as that in the images of Hα line center (see Figure 3(a1)). Around 19:07 UT, a C4.0 flare occurred to the northeast of the filament system and then evolved into three separate compact bright patches (panel (a2)). Meanwhile, another weak brightening appeared at the site on the west of the filament's northern footpoint and then illuminated the whole north part of the filament system around 19:08 UT (panel (a3)). The brightening then propagated laterally along the filament spine and flipped from bottom to top after rounding the turning point of the shape of "7", forming a southeastward material flow. This flow illuminated the southeast narrow region of the filament and the structured distribution of redshift (panel (a4)). About 20 minutes later, a compact brightening was detected beneath the south part of the filament and then the whole filament was activated (panel (a5)), resulting in the final eruption of the upper part of the filament system (panel (a6)). In subsequent AIA 171 and 304 Å observations, we can see that this eruption produced a set of post-flare loops outlining the initial "7" shape of the erupting filament. Moreover, under the post-flare loops, there was still a filament remaining where the erupting one was located (panels (a7) and (a8)). We speculate that it is the material flow in the remaining filament section that produces the region dominated by blueshift in Figure 2.

Along the moving direction of erupting filament section, we also constructed a time-distance map through AIA 304 Å images as shown in Figure 3(b). It is obvious that the south region of the pre-flare filament system was relatively wide in the beginning, which was then activated by surrounding small-scale flare. As a result, the east part (the upper part) of this region was lifted a little while the the west part (the lower part) was intermittently but successively heated, which thus did not show dark absorption features. Subsequently, the upper filament section erupted northeastwards with a typical two-phase evolution: slow rise followed by a rapid eruption. About half an hour after the eruption, the west part (the lower part) of the filament system cooled down and showed dark absorption features again. Combining the Doppler velocity distribution and temporal evolution of the filament, we propose that there were two independent material flow systems within the pre-flare

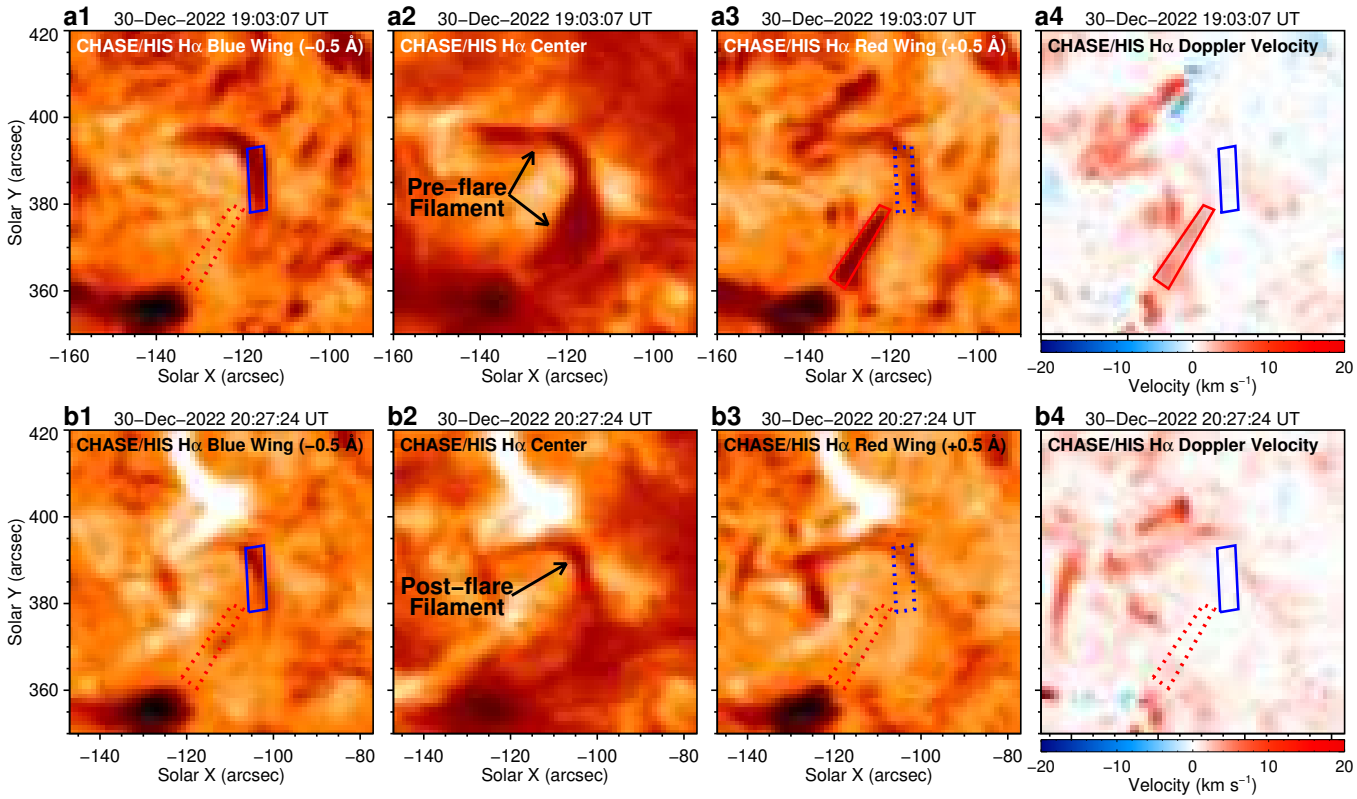

Figure 2. Mass motions of the filaments before and after the partial eruption observed by the *CHASE*/HIS in Hα channel. (a1)–(a4): Images of Hα line center and two wings ($\Delta\lambda = \pm 0.5$ Å) and the corresponding Doppler velocity map derived from Hα spectra data exhibiting the material flows in filaments before the eruption. The blue and red quadrilaterals mark the filament sections dominated by blueshift and redshift, respectively. The choice of solid and dotted lines depends on whether the signal is clear. (b1)–(b4): Similar to (a1)–(a4), but for the filament after the eruption.

filament and the upper part eventually erupted while the lower part remained, which might be supported by two up-and-down MFRs, i.e., double-decker MFR system (Liu et al. 2012).

3.2.2. *Magnetic topology of the double-decker filament system*

To verify the speculation about the double-decker MFR structure, we further extrapolated 3D magnetic topology of the filament system through NLFFF method based on the photospheric vector magnetic fields of *SDO*/HMI at 18:48 UT on 2022 December 30, just before the occurrence of the M3.7 flare. Moreover, we calculated the twist number T_w and the squashing factor Q of the reconstructed fields. Then we can obtain the T_w and Q distribution maps in the photospheric or selected vertical planes. According to the photospheric twist map, we plotted the magnetic field lines across the photosphere where $|T_w| \geq 1.0$ around the footpoint of the filament system. As shown in Figure 4, there are indeed two MFRs in the flare core region: MFR2 with T_w <–1.0 above MFR1 with T_w >1.0, forming a double-decker MFR configuration (Liu et al. 2012). In the south region of this configuration, higher MFR2 is located to the east of MFR1 in the plane of sky (POS). But in the north region, MFR2 passes MFR1 from below and roots in a negative-polarity region located to the west-south of the footpoint of MFR1.

In Figures 5(a)–(b), the heated material flow rotating the filament system is shown clearly. We can see that the flow originated beneath the north part of the filament, then flipped from bottom to top, rotating around the lower filament, and eventually deposited at a site on the east of the filament's southern footpoint. Combining the EUV observations and NLFFF results shown in Figures 3–5, we can conclude that they are consistent with each other according to the following two facts: 1) The extrapolated magnetic structure and the observed filament material flow share similar footpoint positions; 2) MFR2 rotates around MFR1 in their north part in a similar way that the bright flow in the upper filament rotates around the lower filament. As a result, we suggest that MFR2 represents the magnetic structure of the erupting upper filament and MFR1 corresponds to the remaining lower filament. About the consistency between the observations and NLFFF results, we would

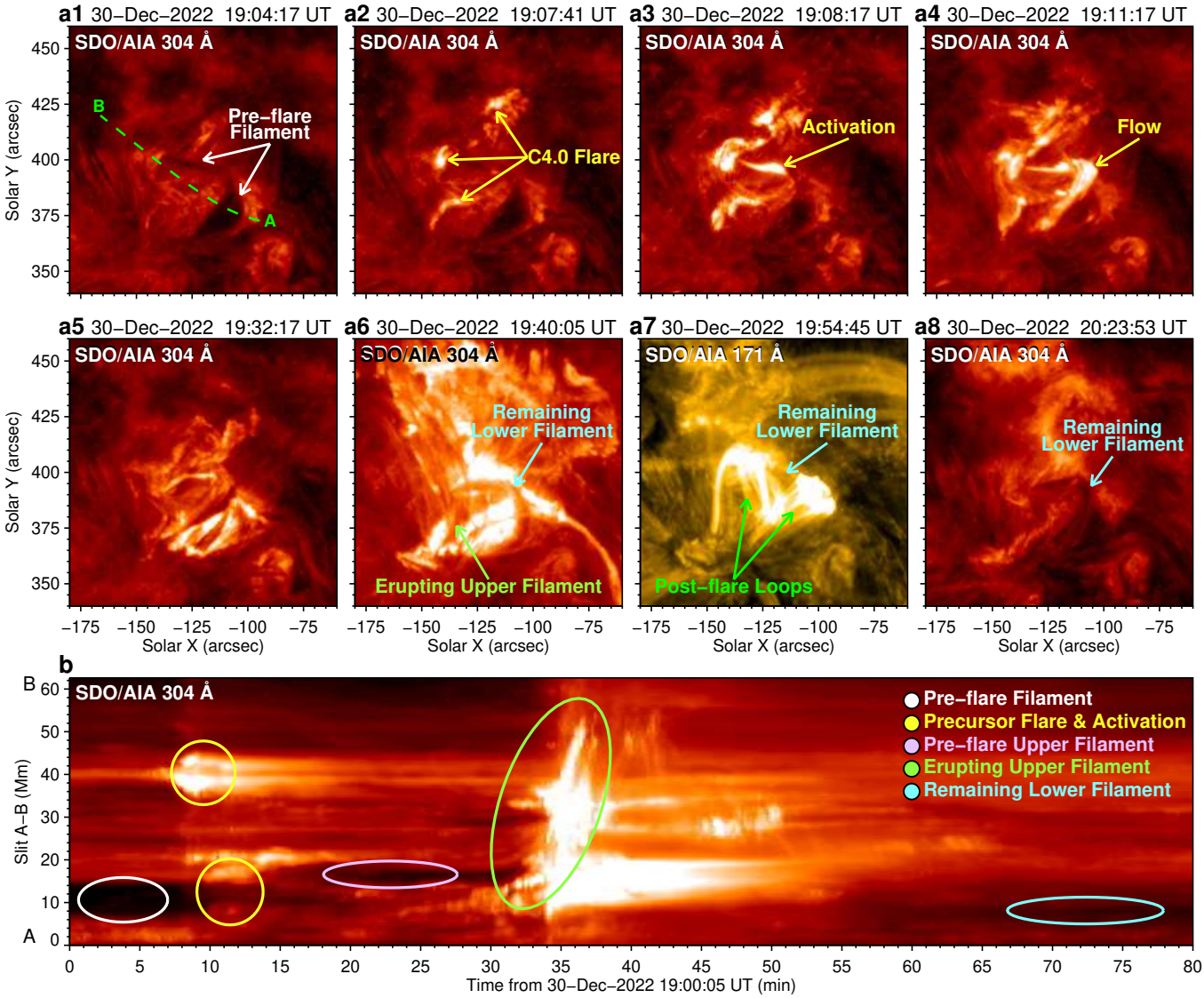

Figure 3. Temporal evolution of the double-decker filament system before and during its partial eruption. (a1)–(a8): Sequence of *SDO*/AIA 304 and 171 Å images showing the partial eruption process of the double-decker filaments and the resultant post-flare loops. The slit "A–B" in (a1) approximates the moving direction of erupting filament section. (b): Time-distance map derived from the 304 Å images along the slit "A–B" shown in (a1).

like to note that the field lines shown here are the magnetic field lines with absolute twist number larger than 1.0, which means that there are still other less twisted field lines of the filament that are not plotted. Therefore, the magnetic structure shown in Figure 4 might not exactly match the observed filament system in space.

Along the green cut marked in Figure 4(a), we make T_w distribution maps in the vertical (x-z) plane and show it in panels (d) and (e). One can see that there are two regions with high positive and negative T_w in this vertical twist map, which correspond to the cross sections of MFR1 and MFR2, respectively. High Q ribbons are located along the edge of the two high twist regions and the interface between them as shown in panel (f). Although the high-Q regions are usually locations favorable for magnetic reconnection, the two MFRs of the double-decker structure reported here have opposite magnetic twist, which means that the field line of the two MFRs at the intersecting boundary between them would have the same direction. As discussed by Pan et al. (2021), such special double-decker topology could be more stable than the magnetic configurations having the same sign of twist originally proposed by Liu et al. (2012) because the two vertically-distributed parts are not separated by a hyperbolic flux tube (HFT) where a current layer likely develops. As a result, it is reasonable that the lower filament of this double-decker configuration apparently did not undergo any significant

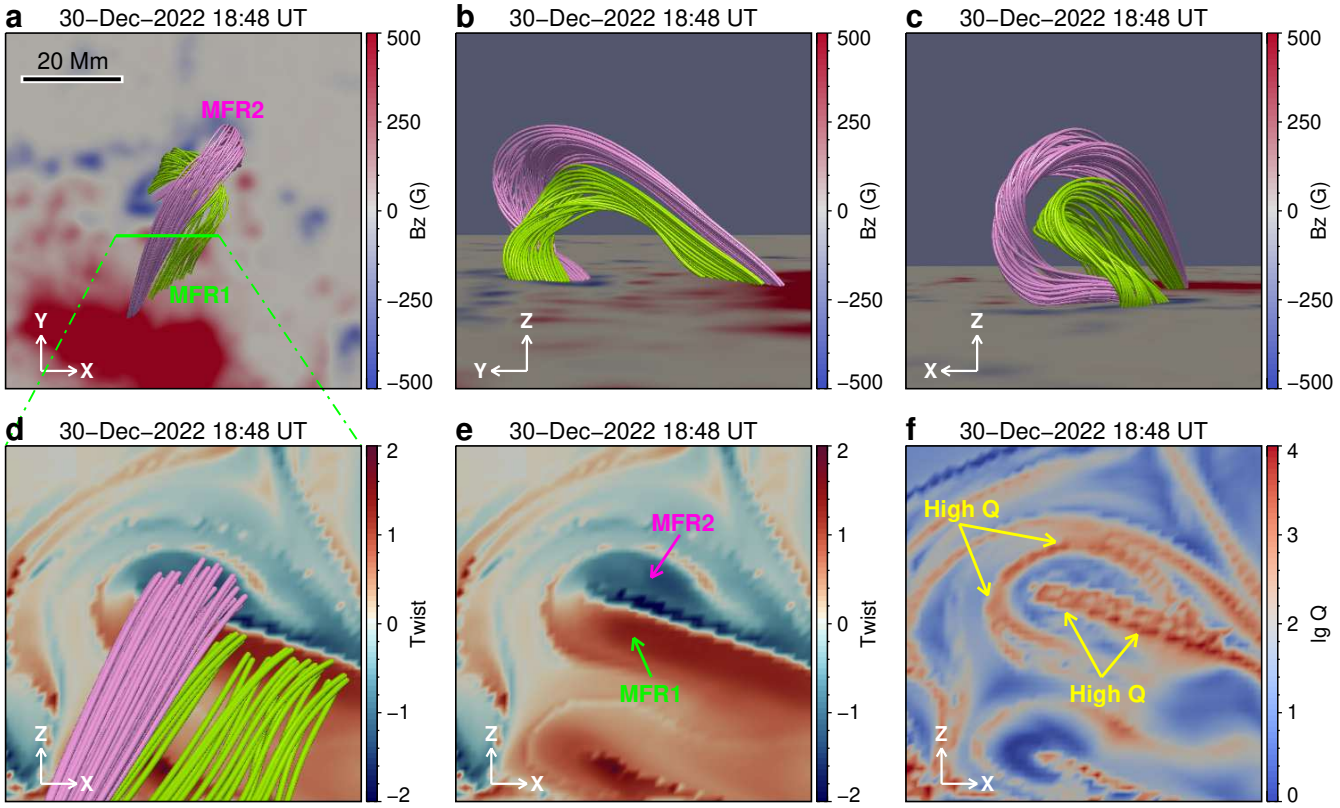

Figure 4. Three-dimensional (3D) magnetic topology of the filaments before the partial eruption revealed by NLFFF extrapolation. (a)–(c): Top and side views of two MFRs (MFR1 and MFR2) composing a double-decker configuration. (d)–(f): Distributions of magnetic twist T_w and logarithmic Q in the vertical plane based on the green cut denoted in (a).

morphological change during the partial eruption. However, during the 20 minutes before the onset of the partial eruption, we noticed that there were frequent local EUV brightenings appearing around the south region of the filament system (Figures 5(c)–(d)), which might be due to the interaction within the two vertically-distributed filaments (or MFRs). Although the precursor event driving the filament partial eruption is an interesting topic, it is beyond the scope of the present work and will be discussed in detail in our future study.

Since the two MFRs composing a double-decker configuration have similar footpoints, it is reasonable to believe that they have the same sign of helicity and are formed successively through similar way, e.g., direct emergence from below the photosphere (Fan 2001; Okamoto et al. 2008), magnetic reconnection of sheared arcades in the corona (van Ballegooijen & Martens 1989; Amari et al. 2003; Cheng et al. 2014), or through splitting process of a single MFR (Gilbert et al. 2001; Kliem et al. 2014; Pan et al. 2021). However, the double-decker configuration reported here consists of two MFRs with opposite magnetic twist, which is not consistent with the magnetic configurations proposed by Liu et al. (2012), where the MFRs or sheared arcades have the same sign of twist. Then, a question naturally arises as to how such double-decker configuration containing two MFRs with opposite twist in equilibrium can form. In the next subsection, we will explore the possible formation of such configuration and try to find observational evidence of the two vertically-distributed filaments of being opposite twist.

3.3. *Formation of the double-decker filament system*

To investigate the formation of the double-decker configuration containing two MFRs with opposite twist, we firstly analyzed the pre-eruption *SDO*/AIA 304, 171 Å observations and *SDO*/HMI LOS magnetograms on 2022 December 30 (see Figure 6 and the corresponding animation). One can see that at the beginning of December 30, there were only several north-south arch filament systems (AFSs) in the region of interest, connecting the sunspot region with positive magnetic polarity and a negative-polarity region to the north of the sunspot (panel (a1)). Then, the east part of north end of these AFSs kept moving northeastwards and the AFSs thus became more and more sheared, which eventually evolved into a filament with a shape of "7" around 13:03 UT (panels (a2)–(a3)). During the following several

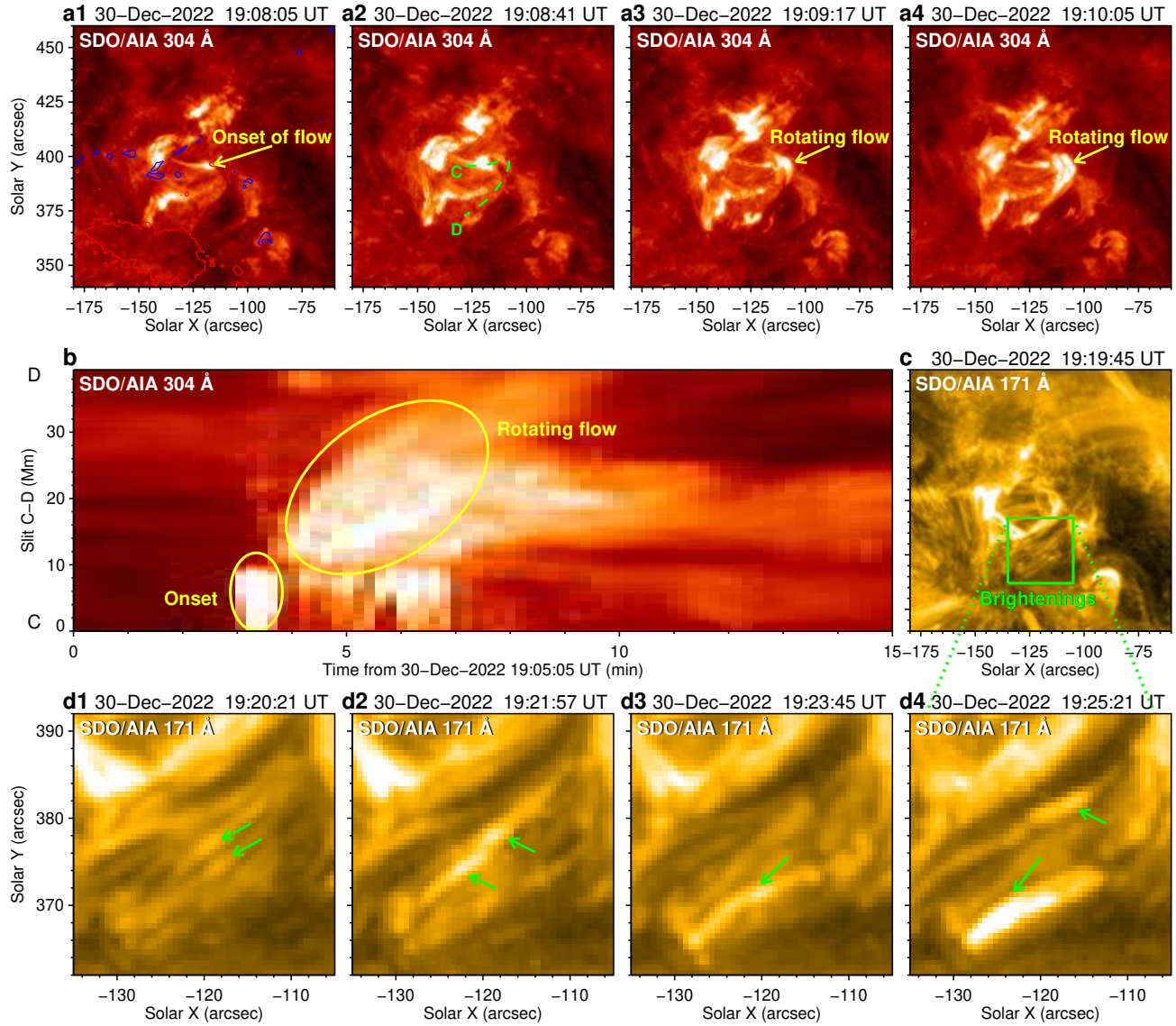

Figure 5. Material flow and transient brightenings within the double-decker filament system before its partial eruption. (a1)–(a4): Sequence of *SDO*/AIA 304 Å images showing the material flow rotating around the lower filament (MFR1). The slit "C–D" in (a2) approximates the moving direction of the flow. (b): Time-distance map derived from the 304 Å images along the slit "C–D" shown in (a2). (c): 304 Å image showing the filament system after being disturbed by the flow. (d1)–(d4): Sequence of *SDO*/AIA 171 Å images showing the frequent brightenings in the south region of the filament system before its eventual eruption.

hours, this filament gradually grew up to have the shape of the pre-flare filament as shown in Figures 2 and 3. As shown in Figure 6(a4), around 16:09 UT, a bright material flow appeared to rotate around the filament, similar to the flow rotating the lower filament occurring before the onset of the filament partial eruption. It indicates that the double-decker configuration had probably completely formed at that time and the flow was along the upper MFR2.

Meanwhile, HMI LOS magnetograms reveal that the negative-polarity region to the north of the sunspot can roughly be divided into two patches: east part and west part (Figure 6(c1)). The east part is the footpoint of the north leg of the filament and kept moving northeastwards while the west part kept moving northwestwards (see the green and red arrows). Small-scale dipolar magnetic fields with direction of west-east successively emerged between the two parts. As a result, the positive patches of the emerging dipolar fields kept cancelling with the existing west part negative fields (see Figures 6(c2)–(c4)). Meanwhile, transient brightenings around sites of the flux cancellation were inter-

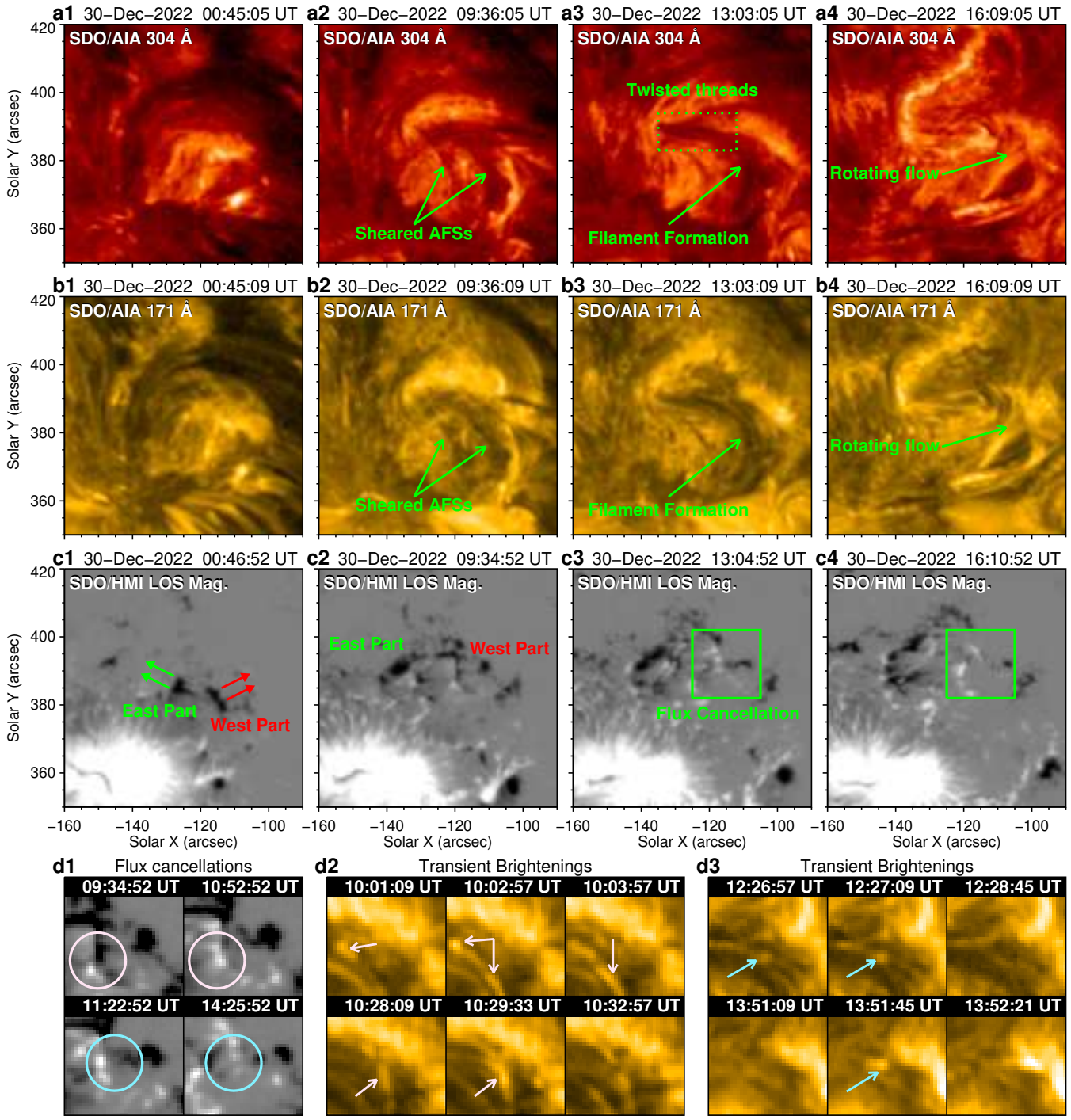

Figure 6. Formation of the double-decker filament system. (a1)–(b4): Sequences of AIA 304 and 171 Å images showing the formation of the double-decker filament system. (c1)–(c4): Sequence of HMI LOS magnetograms exhibiting the opposite shearing motions of the northern footpoints of the initial filament structures and flux cancellation during the double-decker filament formation. The green and red solid arrows in (c1) denote the moving directions of the east and west parts of the northern footpoints. The green squares mark the region where magnetic flux cancellation happens successively, as well as the field view of panels (d1)–(d3). (d1)–(d3): Sequences of HMI LOS magnetograms and AIA 171 Å images exhibiting two flux cancellation processes and associated transient brightenings around the west part of the northern footpoints of the initial filament structures (i.e., the northern footpoint of the initial structure of upper MFR2). The circles and arrows denote the sites of the flux cancellation and brightenings. An animation (Figure6.mp4) of AIA 171, 304 images and HMI LOS magnetograms, covering 00:00 UT to 19:00 UT on December 30, is available in the online journal to present the formation of the double-decker filament system. The animation's duration is 11 seconds.

mittently observed in AIA EUV images (see Figures 6(d1)–(d3)). It is widely accepted that the shearing motion of AFSs observed here would result in the formation of filament through magnetic reconnection between sheared arcades. But such process can not produce a double-decker configuration of two MFRs with opposite magnetic twist as reported here. We speculate that the formation of such double-decker filament system could be caused by another process related to the magnetic flux cancellation and brightenings around the west part negative fields shown in Figures 6(c2)–(d3).

To verify the speculation about the formation of the double-decker structure, we further investigate temporal evolution of 3D magnetic structures of the filament system based on NLFFF extrapolations with a time sequence. Figures 7(a1)–(a4) show that at 09:36 UT on December 30, two sets of twisted magnetic structures with direction of southwest to northeast and positive T_w were extrapolated (see the green lines), corresponding to the two sets of sheared AFSs in the target region. Meanwhile, we should note that there was another sheared structure with a different direction of southeast to northwest and negative T_w (see the pink lines) above the AFS structures. And the northwest footpoint of this upper structure was located at the west negative-polarity patch as shown in Figures 6(c1)–(c2). From Figures 7(b1)–(b4), one can see that, when the sheared AFSs evolved into a "7"-shaped filament at 13:24 UT, a MFR structure with the similar shape and highly positive T_w also formed. As for the magnetic structure with negative T_w at a higher altitude, it became more twisted and its northwest footpoint partially moved to the east negative-polarity region near the north end of the lower MFR. In the meantime, magnetic flux cancellation and the associated EUV brightenings intermittently occurred around the northwest end of this upper twisted structure as shown in Figures 6(d1)–(d3).

Temporal evolution of the filament system shown in Figures 6 and 7 provides critical clues for the formation of the double-decker configuration of two MFRs with opposite magnetic twist. We infer that the two MFRs of the double-decker configuration originated from two magnetic systems with different initial topologies: i.e., different directions, connections, and opposite magnetic twist. But subsequent interactions with the emerging fields changed the magnetic connection of initial structure of the upper MFR2 by moving its north end eastwards to a region near the north end of the lower MFR1. The continuous flux cancellation and associated EUV brightenings around the northwest end of the initial structure of the upper MFR2 (Figures 6(d1)–(d3)) provide a solid evidence for the existence of magnetic reconnection driving the magnetic connection change of MFR2. In this scenario, it is acceptable that MFR1 and MFR2 have opposite magnetic twist when they eventually evolved into a double-decker MFR configuration with similar footpoints. To illustrate more intuitively this physical scenario for the formation of double-decker filament system, we draw a schematic diagram as shown in Figure 8.

It is worth noting that for the large-scale filaments observed by high-resolution ground-based telescopes, one can clearly determine the sign of their magnetic twist according to the filament threads or heated plasma flows along the twisted field lines of the filament. But in the event reported here, the double-decker filaments of interest are small-scale active region filaments and show no obvious signals of twisted threads or flows in the *CHASE* or *SDO* observations. Moreover, because the lower filament was located below the upper one and they were near the solar disk center, it is difficult to determine whether the two parts have opposite twist through the observations from a top-down perspective. However, during the formation process of the double-decker configuration, we find some observational evidence of the two vertically-distributed filaments of being opposite twist as follows: 1) As shown in Figure 6 and the corresponding animation, directions of shearing motion forming the initial structures of lower and upper filaments/MFRs are opposite, which would naturally result in the opposite twist of the two filaments/MFRs. 2) When the upper filament was not formed yet, we find twisted threads of the lower filament with a positive sign of magnetic twist at 13:03:05 UT (Figure 6(a3)), which is consistent with the sign of magnetic twist of the lower MFR revealed by the NLFFF modeling.

Regarding the formation of the double-decker configuration containing two MFRs with the same magnetic twist in equilibrium, Liu et al. (2012) proposed two possible scenarios: (1) After the formation of upper MFR above the PIL, the lower branch emerges from below the photosphere at the same site (hereafter "emerging model"). (2) Both branches originally belong to a single MFR or flux bundle and are then separated into two parts (hereafter "splitting model"). The emerging model can be supported the observations that an MFR can directly emerge under a pre-existing filament (Okamoto et al. 2008). As for the splitting model, it is motivated by the "partial eruption" scenario proposed by Gilbert et al. (2001), in which internal magnetic reconnection within an MFR can split it into two MFRs with the same handedness, and further verified by following observations and numerical modeling results (Kliem et al. 2014; Tian et al. 2018;

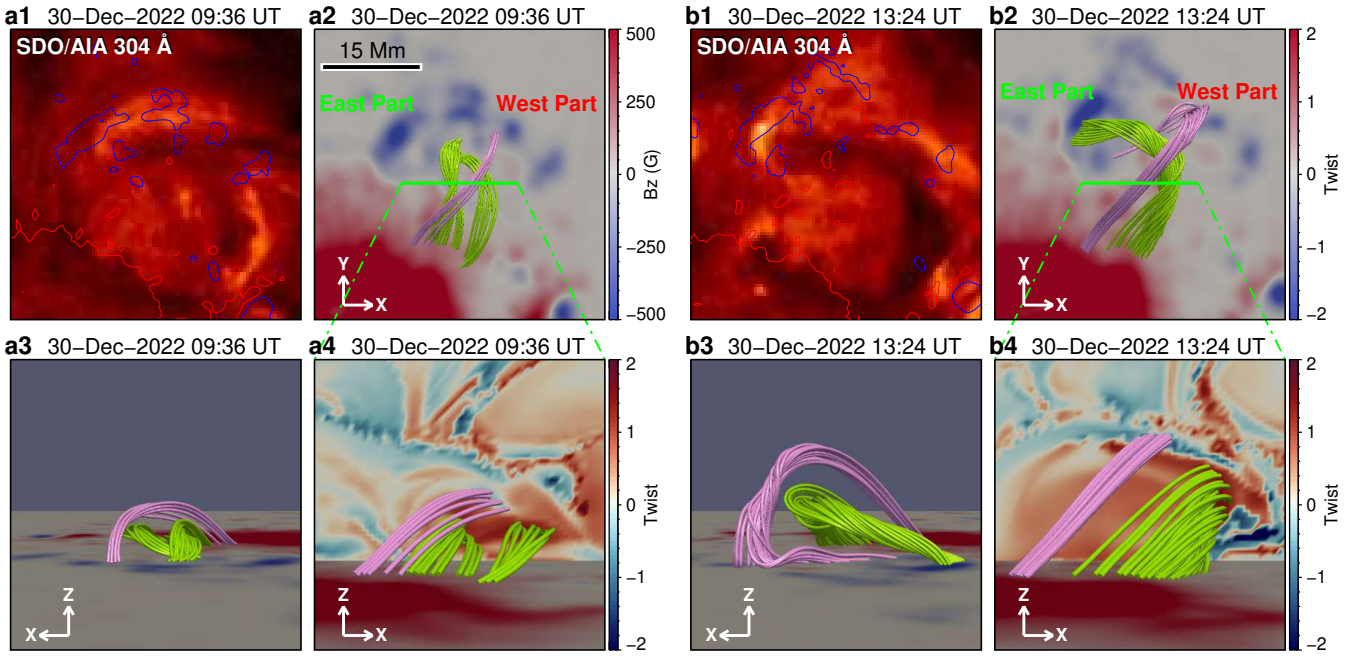

Figure 7. Temporal evolution of magnetic and emission structures during the formation of the double-decker filament. (a1)–(a4): AIA 304 Å image and NLFFF extrapolation results at 09:36 UT exhibiting the filament system and its 3D magnetic topology at the early stage of formation. The green and pink field lines represent initial magnetic topology of lower MFR1 and upper MFR2, respectively. (b1)–(b4): Similar to (a1)–(a4), but for the time point of 13:24 UT at the late stage of formation.

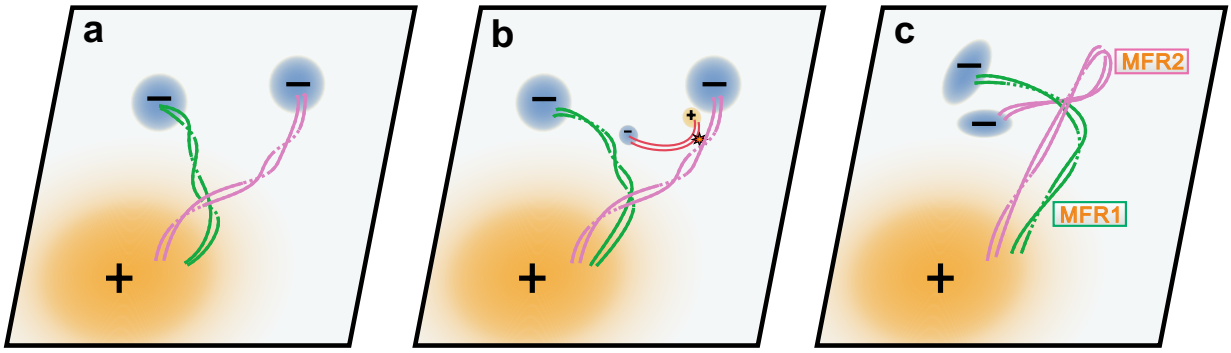

Figure 8. Schematic diagram depicting the formation of double-decker configuration consisting of two MFRs with opposite magnetic twist. The green and pink twisted curves in (a) represent initial magnetic topologies of the two MFRs: lower MFR with direction of north-east to south-west and positive magnetic twist; upper MFR with direction of north-west to south-east and negative magnetic twist. The red curves in (b) delineate emerging dipolar magnetic fields with direction of west-east between the north footpoints of the two MFRs. The star symbol marks the site of magnetic reconnection between the emerging dipolar magnetic fields and the north-west leg of the upper MFR, producing eventually the double-decker configurations consisting of MFR1 and MFR2 with similar footpoints but opposite magnetic twist (see twisted curves in (c)).

Pan et al. 2021). The formation of the initial MFR in the two scenarios can be attributed to the reconnection between two groups of sheared arcades near the PIL driven by shearing, converging, and rotation motions of their magnetic footpoints (Cheng et al. 2014; Yan et al. 2018; Hou et al. 2018; Zhang et al. 2022b). In the present work, we propose another scenario to explain the formation of the double-decker MFRs with opposite magnetic twist reported here. As shown by Figure 8, in this scenario, magnetic reconnection between the newly emerging fields and initial structure of the upper MFR plays a key role in the formation of eventual double-decker configuration by moving the footpoint of the involved MFR. Such footpoint evolution driven by magnetic reconnection between solar filaments and their surrounding structures has been frequently reported (Li et al. 2016; Yang et al. 2017a; Huang et al. 2018; Guo et al. 2021; Song et al. 2023). Moreover, we

suggest that such scenario might also apply to the formation of typical double-decker configuration with the same magnetic twist.

4. SUMMARY

Based on the high-resolution observations from the *CHASE*, *SDO*, and *ASO-S*, we investigate a typical filament partial eruption event, present integrated evidence for the double-decker MFR configuration of pre-eruption filament, and propose a new scenario for its formation. The main results are summarized as follows:

1. On 2022 December 30, a filament was located to the northwest of the main sunspot of NOAA AR 13176 and its subsequent partial eruption produced an M3.7 flare. The *CHASE* Hα spectroscopic observations reveal distinct structured distribution of Doppler velocity within the pre-flare filament, where redshift only appeared in the east narrow part of the south filament region and then disappeared after the partial eruption while the north part dominated by blueshift remained. Combining the Doppler velocity distribution and temporal evolution of the filament, we infer that there were two independent material flow systems within the pre-flare filament, which might be supported by a double-decker configuration.

2. NLFFF extrapolations reveal that there are indeed two vertically-distributed MFRs in the flare core region: MFR2 with T_w <–1.0 above MFR1 with T_w >1.0, forming a double-decker MFR configuration. In the south region of this configuration, higher MFR2 is located to the east of MFR1 in the POS. But in the north region, MFR2 passes MFR1 from below and roots around the footpoint of MFR1. This magnetic configuration is consistent with the observations mentioned above, and we suggest that MFR2 represents the magnetic structure of the erupting upper filament and MFR1 corresponds to the remaining lower filament.

3. The double-decker configuration reported here consists of two MFRs with similar footpoints but opposite magnetic twist. To explain the formation of such type of double-decker MFR configuration, we proposed a new scenario as follows: the two MFRs of this double-decker configuration originate from two magnetic systems with different initial connections and opposite magnetic twist. But subsequent magnetic reconnection between the initial structure of the upper MFR and surrounding newly-emerging fields gradually results in the motion of the footpoint of the upper MFR to a region around the footpoint of the lower MFR, thus leading to the formation of eventual double-decker configuration.

It is worth noting that although the NLFFF extrapolation results and observations of HMI LOS photospheric magnetograms and AIA EUV images support our scenario for the formation of the double-decker MFR configuration reported here, the initial structure of overlying MFR2 is difficult to identify clearly in the AIA observations. The absence of the precursor structure of MFR2 could be caused by its low plasma density at the early stage. After interacting with the lower emerging field filled with plenty of cold plasmas, the newly-formed MFR2 will be injected by a large quantity of heated plasma and then cooled down, forming the upper section of the double-decker filament system distinct in the EUV and Hα imaging observations. In addition, there is another important topic that is not discussed in this paper: how was such double-decker filament system activated and then evolved into partial eruption, producing an M3.7 flare? We have noticed that in AIA EUV observations, there were frequent local brightenings and bright threads appearing in the south region of filament during the 20 minutes before its eventual eruption. The evolution of the double-decker filament system and driving mechanism of its partial eruption will be discussed in detail in our future paper (Paper II, in preparation).

The authors are cordially grateful to the anonymous referee for the constructive comments and suggestions. The data used here are courtesy of the *CHASE*, *ASO-S*, *SDO*, *GOES*, *SUTRI*, and *FY-3E* science teams. The authors are supported by the National Key R&D Program of China (2022YFF0503800, 2022YFF0503000, and 2019YFA0405000), the Strategic Priority Research Program of CAS (XDB0560000 and XDB41000000), the National Natural Science Foundation of China (12273060, 12222306, 12333009, 12127901, 12073042, 12233012, 11921003, and 11903050), "Integration of Space and Ground-based Instruments" project of CNSA, the Youth Innovation Promotion Association CAS (2023063), the Open Research Program of Yunnan Key Laboratory of Solar Physics and Space Science (YNSPCC202211), BJAST Budding Talent Program (23CE-BGS-07), and Yunnan Academician Workstation of Wang Jingxiu (No. 202005AF150025). *CHASE* mission is supported by CNSA. *SDO* is a mission of NASA's Living With a Star Program. *ASO-S* mission is supported by the Strategic Priority Research Program on Space Science of CAS, Grant No. XDA15320000. *SUTRI* is a collaborative project conducted by the National Astronomical Observatories of

CAS, Peking University, Tongji University, Xi'an Institute of Optics and Precision Mechanics of CAS and the Innovation Academy for Microsatellites of CAS.

REFERENCES

Amari, T., Luciani, J. F., Aly, J. J., Mikic, Z., & Linker, J. 2003, ApJ, 585, 1073, doi: 10.1086/345501

Antiochos, S. K., & Klimchuk, J. A. 1991, ApJ, 378, 372, doi: 10.1086/170437

Antolin, P., Okamoto, T. J., De Pontieu, B., et al. 2015, ApJ, 809, 72, doi: 10.1088/0004-637X/809/1/72

Aulanier, G., DeVore, C. R., & Antiochos, S. K. 2002, ApJL, 567, L97, doi: 10.1086/339436

Awasthi, A. K., Liu, R., & Wang, Y. 2019, ApJ, 872, 109, doi: 10.3847/1538-4357/aafdad

Bai, X., Tian, H., Deng, Y., et al. 2023, Research in Astronomy and Astrophysics, 23, 065014, doi: 10.1088/1674-4527/accc74

Berger, T., Hillier, A., & Liu, W. 2017, ApJ, 850, 60, doi: 10.3847/1538-4357/aa95b6

Bi, Y., Jiang, Y., Yang, J., et al. 2015, ApJ, 805, 48, doi: 10.1088/0004-637X/805/1/48

Chen, H., Duan, Y., Yang, J., Yang, B., & Dai, J. 2018, ApJ, 869, 78, doi: 10.3847/1538-4357/aaead1

Chen, J., Su, Y., Liu, R., et al. 2021, ApJ, 923, 142, doi: 10.3847/1538-4357/ac2ba1

Chen, P. F., & Shibata, K. 2000, ApJ, 545, 524, doi: 10.1086/317803

Chen, P.-F., Xu, A.-A., & Ding, M.-D. 2020, Research in Astronomy and Astrophysics, 20, 166, doi: 10.1088/1674-4527/20/10/166

Cheng, X., Ding, M. D., Zhang, J., et al. 2014, ApJ, 789, 93, doi: 10.1088/0004-637X/789/2/93

Cheng, X., Kliem, B., & Ding, M. D. 2018, ApJ, 856, 48, doi: 10.3847/1538-4357/aab08d

Dacie, S., Török, T., Démoulin, P., et al. 2018, ApJ, 862, 117, doi: 10.3847/1538-4357/aacce3

Dai, J., Li, Z., Wang, Y., et al. 2022, ApJ, 929, 85, doi: 10.3847/1538-4357/ac4fbe

Démoulin, P., & Aulanier, G. 2010, ApJ, 718, 1388, doi: 10.1088/0004-637X/718/2/1388

Deng, Y.-Y., Zhang, H.-Y., Yang, J.-F., et al. 2019, Research in Astronomy and Astrophysics, 19, 157, doi: 10.1088/1674-4527/19/11/157

Fan, Y. 2001, ApJL, 554, L111, doi: 10.1086/320935

Gan, W., Zhu, C., Deng, Y., et al. 2023, SoPh, 298, 68, doi: 10.1007/s11207-023-02166-x

Gibson, S. E., & Fan, Y. 2006, ApJL, 637, L65, doi: 10.1086/500452

Gilbert, H. R., Alexander, D., & Liu, R. 2007, SoPh, 245, 287, doi: 10.1007/s11207-007-9045-z

Gilbert, H. R., Holzer, T. E., & Burkepile, J. T. 2001, ApJ, 549, 1221, doi: 10.1086/319444

Gilbert, H. R., Holzer, T. E., Burkepile, J. T., & Hundhausen, A. J. 2000, ApJ, 537, 503, doi: 10.1086/309030

Guo, Y., Hou, Y., Li, T., & Zhang, J. 2021, ApJ, 920, 77, doi: 10.3847/1538-4357/ac1ac6

Guo, Y., Schmieder, B., Démoulin, P., et al. 2010, ApJ, 714, 343, doi: 10.1088/0004-637X/714/1/343

Hou, Y., Zhang, J., Li, T., & Yang, S. 2020a, in Solar and Stellar Magnetic Fields: Origins and Manifestations, ed. A. Kosovichev, S. Strassmeier, & M. Jardine, Vol. 354, 443–447, doi: 10.1017/S1743921319009967

Hou, Y. J., Li, T., Song, Z. P., & Zhang, J. 2020b, A&A, 640, A101, doi: 10.1051/0004-6361/202038348

Hou, Y. J., Zhang, J., Li, T., Yang, S. H., & Li, X. H. 2018, A&A, 619, A100, doi: 10.1051/0004-6361/201732530

Hu, H., Liu, Y. D., Chitta, L. P., Peter, H., & Ding, M. 2022, ApJL, 940, L12, doi: 10.3847/2041-8213/ac9dfd

Huang, Z., Mou, C., Fu, H., et al. 2018, ApJL, 853, L26, doi: 10.3847/2041-8213/aaa88c

Jenkins, J. M., & Keppens, R. 2022, Nature Astronomy, 6, 942, doi: 10.1038/s41550-022-01705-z

Ji, H., Wang, H., Schmahl, E. J., Moon, Y. J., & Jiang, Y. 2003, ApJL, 595, L135, doi: 10.1086/378178

Kliem, B., Török, T., Titov, V. S., et al. 2014, ApJ, 792, 107, doi: 10.1088/0004-637X/792/2/107

Lemen, J. R., Title, A. M., Akin, D. J., et al. 2012, SoPh, 275, 17, doi: 10.1007/s11207-011-9776-8

Li, C., Fang, C., Li, Z., et al. 2022, Science China Physics, Mechanics, and Astronomy, 65, 289602, doi: 10.1007/s11433-022-1893-3

Li, D., Shen, Y., Ning, Z., Zhang, Q., & Zhou, T. 2018, ApJ, 863, 192, doi: 10.3847/1538-4357/aad33f

Li, L., Zhang, J., Peter, H., et al. 2016, Nature Physics, 12, 847, doi: 10.1038/nphys3768

Li, T., & Zhang, J. 2012, ApJL, 760, L10, doi: 10.1088/2041-8205/760/1/L10

Li, Y., & Ding, M. D. 2017, ApJ, 838, 15, doi: 10.3847/1538-4357/aa6348

Lin, J., & Forbes, T. G. 2000, J. Geophys. Res., 105, 2375, doi: 10.1029/1999JA900477

Liu, Q., Tao, H., Chen, C., et al. 2022, Science China Physics, Mechanics, and Astronomy, 65, 289605, doi: 10.1007/s11433-022-1917-1
Liu, R., Kliem, B., Török, T., et al. 2012, ApJ, 756, 59, doi: 10.1088/0004-637X/756/1/59
Liu, R., Kliem, B., Titov, V. S., et al. 2016, ApJ, 818, 148, doi: 10.3847/0004-637X/818/2/148
Mackay, D. H., Karpen, J. T., Ballester, J. L., Schmieder, B., & Aulanier, G. 2010, SSRv, 151, 333, doi: 10.1007/s11214-010-9628-0
Mitra, P. K., Joshi, B., Veronig, A. M., et al. 2020, ApJ, 900, 23, doi: 10.3847/1538-4357/aba900
Monga, A., Sharma, R., Liu, J., et al. 2021, MNRAS, 500, 684, doi: 10.1093/mnras/staa2902
Myers, C. E., Yamada, M., Ji, H., et al. 2015, Nature, 528, 526, doi: 10.1038/nature16188
Okamoto, T. J., Tsuneta, S., Lites, B. W., et al. 2008, ApJL, 673, L215, doi: 10.1086/528792
Oliver, R., & Ballester, J. L. 2002, SoPh, 206, 45, doi: 10.1023/A:1014915428440
Pan, H., Liu, R., Gou, T., et al. 2021, ApJ, 909, 32, doi: 10.3847/1538-4357/abda4e
Pesnell, W. D., Thompson, B. J., & Chamberlin, P. C. 2012, SoPh, 275, 3, doi: 10.1007/s11207-011-9841-3
Priest, E. R., & Forbes, T. G. 2002, A&A Rv, 10, 313, doi: 10.1007/s001590100013
Qiu, Y., Rao, S., Li, C., et al. 2022, Science China Physics, Mechanics, and Astronomy, 65, 289603, doi: 10.1007/s11433-022-1900-5
Schmieder, B., Démoulin, P., & Aulanier, G. 2013, Advances in Space Research, 51, 1967, doi: 10.1016/j.asr.2012.12.026
Schou, J., Scherrer, P. H., Bush, R. I., et al. 2012, SoPh, 275, 229, doi: 10.1007/s11207-011-9842-2
Shen, Y., Liu, Y., Liu, Y. D., et al. 2015, ApJL, 814, L17, doi: 10.1088/2041-8205/814/1/L17
Song, Q., Wang, J.-S., Zhang, X., et al. 2023, arXiv e-prints, arXiv:2309.09414, doi: 10.48550/arXiv.2309.09414
Song, Z., Hou, Y., Zhang, J., & Wang, P. 2020, ApJ, 892, 79, doi: 10.3847/1538-4357/ab77b3
Sterling, A. C., & Moore, R. L. 2004, ApJ, 602, 1024, doi: 10.1086/379763
Sun, Z., Li, T., Tian, H., et al. 2023, ApJ, 953, 148, doi: 10.3847/1538-4357/ace5b1
Tian, Z., Shen, Y., & Liu, Y. 2018, NewA, 65, 7, doi: 10.1016/j.newast.2018.05.005
Török, T., & Kliem, B. 2005, ApJL, 630, L97, doi: 10.1086/462412
Tripathi, D., Gibson, S. E., Qiu, J., et al. 2009, A&A, 498, 295, doi: 10.1051/0004-6361/200809801
Tripathi, D., Reeves, K. K., Gibson, S. E., Srivastava, A., & Joshi, N. C. 2013, ApJ, 778, 142, doi: 10.1088/0004-637X/778/2/142
van Ballegooijen, A. A., & Martens, P. C. H. 1989, ApJ, 343, 971, doi: 10.1086/167766
Wang, J., Yan, X., Xue, Z., et al. 2022, A&A, 659, A76, doi: 10.1051/0004-6361/202142584
Wiegelmann, T. 2004, SoPh, 219, 87, doi: 10.1023/B:SOLA.0000021799.39465.36
Wiegelmann, T., Inhester, B., & Sakurai, T. 2006, SoPh, 233, 215, doi: 10.1007/s11207-006-2092-z
Wiegelmann, T., Thalmann, J. K., Inhester, B., et al. 2012, SoPh, 281, 37, doi: 10.1007/s11207-012-9966-z
Xia, C., Chen, P. F., Keppens, R., & van Marle, A. J. 2011, ApJ, 737, 27, doi: 10.1088/0004-637X/737/1/27
Xue, Z., Yan, X., Wang, J., et al. 2023, ApJ, 945, 5, doi: 10.3847/1538-4357/acb8ad
Yan, X., Xue, Z., Cheng, X., et al. 2020, ApJ, 889, 106, doi: 10.3847/1538-4357/ab61f3
Yan, X. L., Wang, J. C., Pan, G. M., et al. 2018, ApJ, 856, 79, doi: 10.3847/1538-4357/aab153
Yang, L., Yan, X., Li, T., Xue, Z., & Xiang, Y. 2017a, ApJ, 838, 131, doi: 10.3847/1538-4357/aa653a
Yang, S., Zhang, J., Zhu, X., & Song, Q. 2017b, ApJL, 849, L21, doi: 10.3847/2041-8213/aa9476
Zhang, J., Wang, J., Deng, Y., & Wu, D. 2001, ApJL, 548, L99, doi: 10.1086/318934
Zhang, P., Hu, X., Lu, Q., et al. 2022a, Advances in Atmospheric Sciences, 39, 1, doi: 10.1007/s00376-021-1304-7
Zhang, Q. M., Ning, Z. J., Guo, Y., et al. 2015, ApJ, 805, 4, doi: 10.1088/0004-637X/805/1/4
Zhang, Y., Yan, X., Wang, J., et al. 2022b, ApJ, 933, 200, doi: 10.3847/1538-4357/ac7391
Zheng, R., Yang, S., Rao, C., et al. 2019, ApJ, 875, 71, doi: 10.3847/1538-4357/ab0f3f
Zhou, Y. H., Chen, P. F., Hong, J., & Fang, C. 2020, Nature Astronomy, 4, 994, doi: 10.1038/s41550-020-1094-3
Zhu, C., & Alexander, D. 2014, SoPh, 289, 279, doi: 10.1007/s11207-013-0349-x
Zirker, J. B., Engvold, O., & Martin, S. F. 1998, Nature, 396, 440, doi: 10.1038/24798
Zou, P., Jiang, C., Wei, F., et al. 2020, ApJ, 890, 10, doi: 10.3847/1538-4357/ab6aa8